Advances in Water Resources 95 (2016) 329–340

Contents lists available at ScienceDirect

Advances in Water Resources

journal homepage: www.elsevier.com/locate/advwatres

The impact of porous media heterogeneity on non-Darcy flow behaviour from pore-scale simulation

Bagus P. Muljadi*, Martin J. Blunt, Ali Q. Raeini, Branko Bijeljic

Department of Earth Science and Engineering, Imperial College, London SW7 2BP, UK

ARTICLE INFO

Article history:
Available online 29 May 2015

Keywords:
Non-Darcy flow
3-D X-ray images
Direct simulation
Heterogeneous porous media

ABSTRACT

The effect of pore-scale heterogeneity on non-Darcy flow behaviour is investigated by means of direct flow simulations on 3-D images of a beadpack, Bentheimer sandstone and Estaillades carbonate. The critical Reynolds number indicating the cessation of the creeping Darcy flow regime in Estaillades carbonate is two orders of magnitude smaller than in Bentheimer sandstone, and is three orders of magnitude smaller than in the beadpack. It is inferred from the examination of flow field features that the emergence of steady eddies in pore space of Estaillades at elevated fluid velocities accounts for the early transition away from the Darcy flow regime. The non-Darcy coefficient β, the onset of non-Darcy flow, and the Darcy permeability for all samples are obtained and compared to available experimental data demonstrating the predictive capability of our approach. X-ray imaging along with direct pore-scale simulation of flow provides a viable alternative to experiments and empirical correlations for predicting non-Darcy flow parameters such as the β factor, and the onset of non-Darcy flow.

1. Introduction

In the creeping flow regime in porous media, the relation between pressure p and the volumetric velocity vector $\mathbf{U} = \frac{\mathbf{q}}{A}$, where $\mathbf{q}$ is the volume flowing per unit time and A is the cross-sectional area of the samples sliced perpendicular to the flow direction, is described by the linear Darcy equation:

$$-\nabla p = \frac{\mu}{\mathbf{K_D}}\mathbf{U}, \tag{1}$$

where μ is the dynamic viscosity of the fluid and $\mathbf{K_D}$ is the Darcy permeability tensor. Such linearity is a direct consequence of Stokes flow where the non-linear inertial term is neglected.

As the flow rate increases, Eq. (1) no longer holds; the relation between p and $\mathbf{U}$ becomes non-linear due to emerging inertial effects and the flow enters the non-Darcy regime. A quadratic term was included by Dupuit [1] and Forchheimer [2] as a correction to the Darcy equation to give what is known as the Forchheimer equation:

$$-\nabla p = \frac{\mu}{\mathbf{K_F}}\mathbf{U} + \beta\rho|\mathbf{U}|^2\mathbf{n}, \tag{2}$$

where $\mathbf{n}$ is a unit vector in the direction of ∇p. $\mathbf{K_F}$ is the Forchheimer permeability tensor which is close to but not equal to $\mathbf{K_D}$, and ρ is the density of the fluid. The additional term in the Forchheimer equation (2) is proportional to the non-Darcy coefficient β.

The onset of non-Darcy flow and the β coefficient in porous media are generally determined by multi-rate pressure test results. These results have been used to develop empirical correlations to predict the β factor [3–7]; yet, given the heterogeneous nature of most reservoir rocks, it is expected that these correlations yield uncertain predictions for samples where direct experimental data is unavailable [8,9].

Numerical simulations are intended to circumvent this problem and provide a microscopic insight into pore-scale flow phenomena by solving the fluid equations directly within the pore spaces of rocks. However, the complexity of the pore geometry and the need to compute flow accurately over a representative element of volume has hitherto limited the application of this approach. Several numerical studies on simplified media and sphere packs have been reported. Fourar et al. [10] used a commercial finite-element method (Femlab) to simulate and predict the onset of non-Darcy flow of Newtonian fluid through 2-D and 3-D periodic sphere packs. Newman and Yin [11] applied the lattice Boltzmann method to predict the onset of non-Darcy flow and the dimensionless inertial resistance factor $\beta\sqrt{\mathbf{K_D}}$, for synthetic 2-D media. They showed that a large contrast between pore and throat size is responsible for an early transition to the inertial regime. Thauvin and Mohanty [12] developed a pore-level network model to describe high velocity flow. They input pore

* Corresponding author. Tel.: +447475834586.
E-mail address: b.muljadi@imperial.ac.uk (B.P. Muljadi).

http://dx.doi.org/10.1016/j.advwatres.2015.05.019

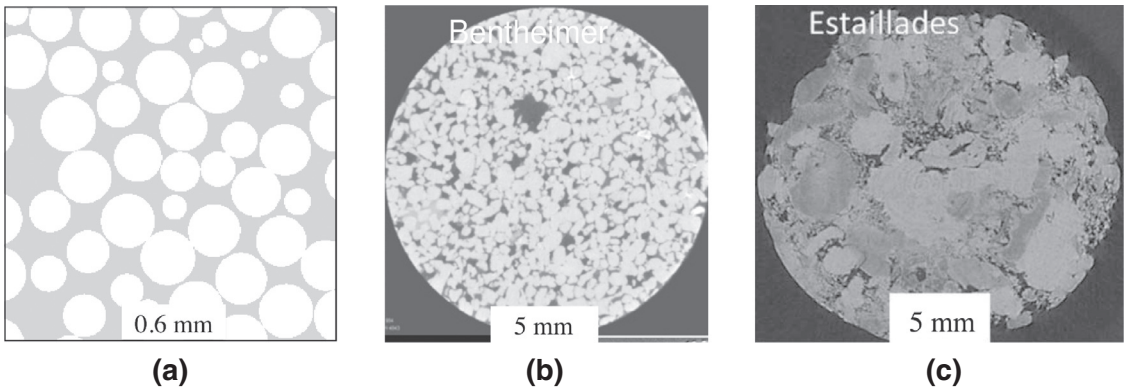

Fig. 1. 2-D cross sections of 3-D grey-scale images of (a) beadpack, (b) Bentheimer, and (c) Estaillades with resolutions of 2 μm, 3.0035 μm, and 3.3113 μm respectively.

size distributions and network coordination numbers into the model, and output permeability, β, tortuosity, and porosity.

In the works of Bijeljic et al. [13,14] the correlation between pore heterogeneity and flow heterogeneity such as probability of molecular displacement and probability density function (PDF) of velocity was elucidated for a range of samples of carbonates and sandstones including Bentheimer and Estaillades. Likewise, in [15,16], Siena et al. and Hyman et al. had attempted to quantify the heterogeneity in the flow and related it to the heterogeneity of pore structures. In this paper, we aim to demonstrate the effect of pore heterogeneities on the onset of non-Darcy flow. Such onset can be identified by the deviation of apparent permeabilities from Darcy permeability, marked by the increase of tortuosity at elevated flow velocities.

In recent years, several studies have been conducted on realistic 3-D images. For instance, Sukop et al. [17] simulated 3-D flows in biogenic vuggy macropore representing subsamples of a karstic Biscayne aquifer with up to 81% macro-porosity to compute the β factor. Their simulations were performed in grids containing 336 × 336 × 336 voxels. Chukwudozie et al. [18] used the lattice Boltzmann method to predict β, permeability and tortuosity of Castlegate sandstone with 0.15–0.18 mm grains and 18% porosity imaged at 7.57 mm resolution using a 3-D image of 300 × 300 × 300 voxels. They compared the computed β factor to experimental data and found a good agreement. However, none of the numerical works above has addressed and demonstrated the effect of pore-scale heterogeneity on the onset of non-Darcy flow and β factor in the range of natural porous media.

In this paper we employ a finite-volume method for simulating fluid flows directly on 3-D images of three porous media with various pore complexity and heterogeneity i.e. a bead (sphere) pack, Bentheimer sandstone and Estaillades carbonate. By conducting the simulations directly in the pore-space images, we are able to examine the key features of the flow fields within these samples as they transition into the non-Darcy regime. The results enable us to better understand the underlying physics of, and the effect of heterogeneities on, the onset of non-Darcy flow.

In the next sections, the physical properties of the samples used in this paper are presented. We then explain the definition of the onset of non-Darcy flow and the Reynolds number used to indicate the cessation of the Darcy flow regime. The results of our numerical simulations are given, discussed and compared to available experimental data.

2. Theoretical background and methodology

2.1. Images and physical properties of the samples

The non-Darcy flows are simulated in pore-space images of three porous media with increasing pore-scale heterogeneity namely: (1) beadpack, (2) Bentheimer sandstone, and (3) Estaillades carbonate. The beadpack image is based on the measurements of the coordinates of the centres of equally-sized spherical grains in a random close packing (see Finney [19]) for which the segmentation into an image has been performed by Prodanović and Bryant [20].

Guadagnini et al. [21] have analysed the statistical scaling of structural attributes of similar Estaillades limestone and Bentheimer sandstone images to those analyzed here. In their study, directional distributions of porosity and specific surface area, which are key Minkowski functionals (geometric observables, see [22]) were employed to describe the pore-space structure. They found that Estaillades displayed characteristics of a more heterogeneous pore space than Bentheimer. The same conclusion was reached by Bijeljic et al. [13,14] who studied the distribution of local flow speeds in the pore space.

The dry-scan images of Bentheimer sandstone [13] and Estaillades carbonate [14] were acquired on a cylindrical core of 5 mm diameter and 25 mm length with an Xradia Versa micro-CT scanner. Bentheimer sandstone image was provided by iRock Technologies, while Estaillades carbonate was acquired in-house. After using a non-local means edge preserving filter (see Buades et al. [23,24]) to reduce noise, the segmentation into binary images was performed using a seeded watershed algorithm based on the three-dimensional gradient magnitude and grey-scale value of each voxel [25]. All image processing was conducted using the Avizo Fire 7.0 program (VSG; http://www.vsg3d.com). In Fig. 1, 2-D cross sections of the 3-D grey-scale images of the beadpack, Bentheimer sandstone and Estaillades carbonates are shown. 3-D voxelised pore spaces of these samples through which the flows are simulated are then generated based on these images.

The resolution of the images, porosity ϕ, characteristic length L of the samples, the total number of voxels and number of pore voxels are all given in Table 1. Note that for unconsolidated porous media such as a beadpack, the diameter of the bead $D_{\text{bead}} = 100\,\mu\text{m}$ is chosen as the characteristic length L. For Bentheimer and Estaillades, the characteristic lengths are estimated as $L \approx \frac{\pi}{S_v}$, S_v is the specific surface area of the pore–grain interface (surface area divided by the total volume − pore plus grain) [26]. The area S_v is measured directly on the image from the number of voxel faces separating void from grain. This method is employed for consolidated media where it is not possible to extract an unambiguous mean grain size.

2.2. Governing equation and numerical method

Flow through the pore spaces of porous media is governed by the incompressible Navier–Stokes equation formulated as:

$$\rho\left(\frac{\partial \mathbf{u}}{\partial t} + \mathbf{u}\cdot\nabla\mathbf{u}\right) = -\nabla p + \mu\nabla^2\mathbf{u},$$
$$\nabla\cdot\mathbf{u} = 0,$$
$$\mathbf{u} = 0, \quad \text{on grain boundaries.} \tag{3}$$

Table 1
Description of the images of beadpack, Bentheimer and Estaillades. For the beadpack, the particle diameter $D_{\text{bead}} = 100\,\mu\text{m}$ is taken as the characteristic length L. For Bentheimer and Estaillades, L is estimated and defined in Section 2.1.

Sample	Resolution (μm)	Porosity, ϕ	L (μm)	Total voxels	Pore voxels
Beadpack	2.0	0.359	100	$300 \times 300 \times 300$	9,700,082
Bentheimer	3.0035	0.211	139.9	$500 \times 500 \times 500$	26,413,875
Estaillades	3.3113	0.108	253.2	$500 \times 500 \times 500$	13,522,500

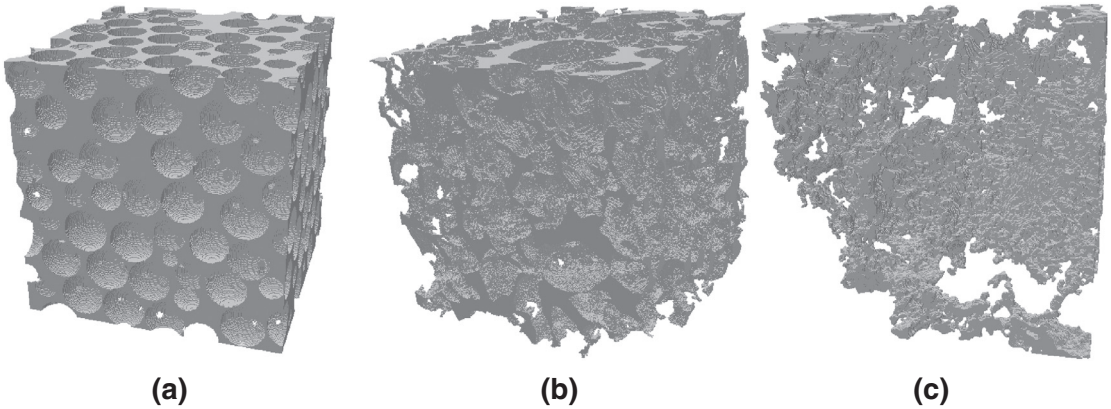

Fig. 2. Voxelised pore spaces of (a) beadpack, (b) Bentheimer, and (c) Estaillades through which the flows are simulated.

Here $\mathbf{u}$ is the velocity vector, and p is pressure. We are interested in the steady-state solution of Eq. (4) i.e., $\frac{\partial \mathbf{u}}{\partial t} = 0$.

Pressure and velocity in Eqs. (4) are solved directly on voxelised pore spaces of the beadpack, Bentheimer and Estaillades as illustrated in Fig. 2, using the pressure implicit with splitting operators (PISO) algorithm by Issa [27]. The numerical solver used in this paper is built upon OpenFOAM, the open source CFD toolbox for solving Navier–Stokes equations, as described in [13,28]. Our criterion for steady state convergence is $\epsilon \leq 10^{-6}$ where $\epsilon = \frac{\|u^n - u^{n-1}\|}{\|u^n\|}$ and $\|\cdot\| = \sqrt{\sum_i (\cdot)_i^2}$. $\{u\}_i^n$ is the discretised magnitude of velocity at the centre of voxel $i = \{1, \ldots, N_{\text{vox}}\}$ at time level n where N_{vox} is the total number of pore voxels. The time difference operator $\partial(\ldots)/\partial t$ is solved with an implicit, first order accurate Euler scheme. The first order accuracy in time is deemed sufficient given that we are interested only in the steady state solution [29,30]. The divergence operator $\nabla \cdot (\ldots)$ is discretised with a Gauss scheme and interpolated using a second order accurate self-filtered central difference scheme, see [31,32].

In all simulations, the boundary condition at the pore-solid interface is set to be a no-slip (zero normal and tangential velocity) boundary condition. A constant pressure boundary condition at the inlet and the outlet faces of the images is used, whereas no-slip boundary conditions are applied on the remaining faces. Water is set as the working fluid with viscosity $\mu = 0.001$ kg/m s and density $\rho = 1000$ kg/m^3. An Intel Xeon E5-2695 2.40 GHz 30 MB cache is used. Each simulation is run in parallel on 16 nodes. The flow computation for the $500 \times 500 \times 500$ cell Estaillades model, the most difficult case, at $Re_K = 3.17 \times 10^{-7}$ requires 3 h 37 min of computer time. The definition of Re_K is given in Section 2.4.

2.3. Permeability

The components of second rank tensor $\mathbf{K} = K_{ij}$, where $i, j = 1, 2, 3$ can be acquired by employing Darcy law

$$K_{ij} = \frac{\mu}{\Delta p_j} U_i, \tag{4}$$

where Δp_j is the pressure gradient in the jth direction, and U_i is the ith component of $\mathbf{U}$ which can be obtained from

$$U_i = \frac{1}{\Omega} \int_\Omega u_i \, d\Omega, \tag{5}$$

where Ω is the volume of the pore space [33].

In this paper, we compute only permeabilities of the porous media contributing to flows in the direction of applied pressure gradients; hence for simplicity, from here-on we denote volumetric velocity as U and permeability simply as K. At the millimetre scale these samples have an approximately isotropic permeability [26].

2.4. Criteria for non-Darcy flow and the β factor

There has been a debate regarding whether or not there is a critical Reynolds number above which the Darcy flow regime ceases to apply [6]. As pointed out by Chhabra [34] in his work on single-phase non-Newtonian fluid flow in porous media and packed beds, there is no clear-cut definition of critical Reynolds number indicating the end of the Darcy flow regime. Comiti et al. [35], however, proposed two limits namely: (1) For engineering purposes, the end of the creeping flow regime to be defined as the moment when the pressure drop due to the linear term becomes less than 95% of the total; (2) A more stringent limit when the pressure drop due to the linear term becomes less than 99%. In this paper, the latter limit is used, after which the Forchheimer regime is assumed.

In regards to the prediction of the onset of non-Darcy flow, several authors have proposed different definitions of Reynolds number [36]. We use two formulations of Reynolds number; the first is the standard definition of Reynolds number based on characteristic length L i.e.,

$$Re_L = \frac{\rho U L}{\mu}. \tag{6}$$

The second formulation is

$$Re_K = \frac{\rho U \sqrt{K_D}}{\mu}, \tag{7}$$

where $\sqrt{K_D}$ is referred to as the Brinkman screening length [37].

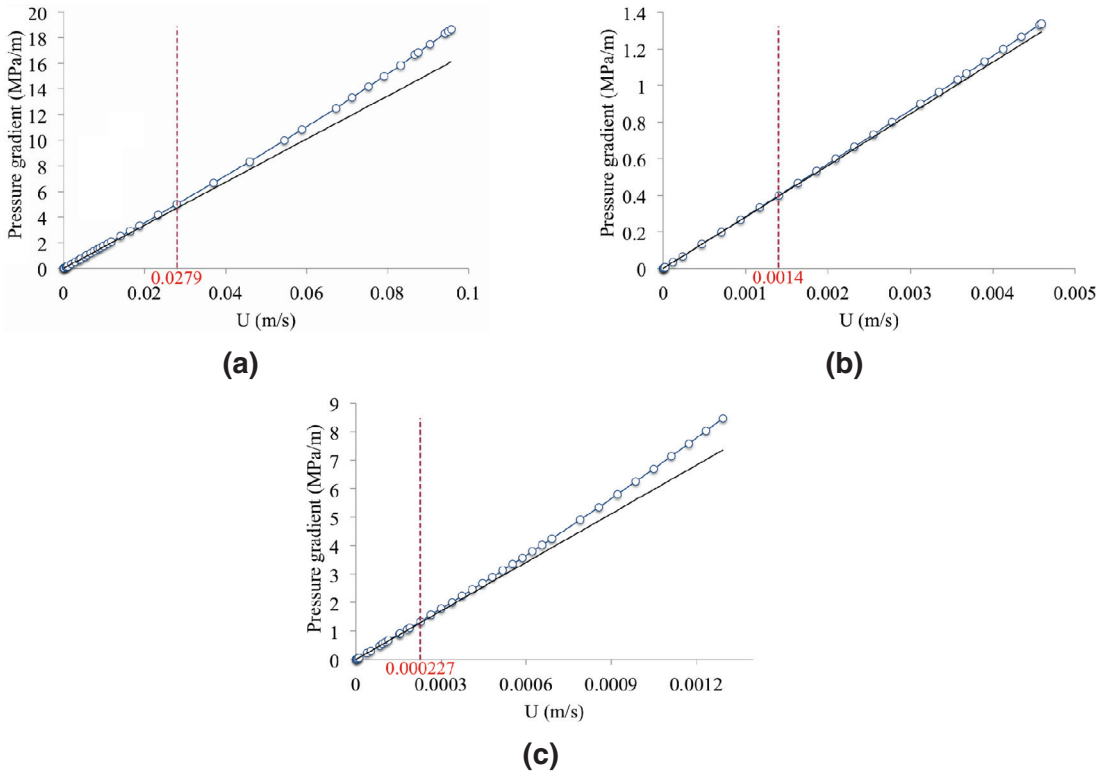

Fig. 3. Computations of pressure gradient for (a) the beadpack, (b) Bentheimer, and (c) Estaillades as they diverge from the Darcy linear relationship with velocity at higher velocities. The symbol ○ represents the observed pressure gradient whereas the black line represents the gradient assuming a linear dependence as $\frac{\mu U}{K_D}$; both as functions of the Darcy or volumetric velocity U. The red dashed lines indicate the onset of the non-Darcy regime where the pressure gradient due to linear term becomes less than 99% of the total. (For interpretation of the references to colour in this figure legend, the reader is referred to the web version of this article.)

We define the dimensionless apparent permeability K^* formulated as:

$$K^* = \frac{K_{\text{app}}}{K_D} \tag{8}$$

to highlight the transition from Darcy to non-Darcy flows. The apparent permeability K_{app} is formulated as

$$\frac{1}{K_{\text{app}}} = \frac{1}{K_F} + \beta \frac{\rho U}{\mu}. \tag{9}$$

By substituting Eq. (8) into Eq. (1), and considering the criterion for the onset of non-Darcy flow defined earlier, it can be inferred that the onset of non-Darcy flow, which will be used throughout this paper, is the point when $K^* = 0.99$. The beta factor β is deduced from the slope of the Forchheimer graph i.e., by plotting the inverse of apparent permeability $\frac{1}{K_{\text{app}}}$ against $\frac{\rho U}{\mu}$ in the Forchheimer regime.

3. Numerical results and discussion

To investigate non-Darcy flow behaviour, we performed simulations of flows with different pressure gradients through the pore spaces of the beadpack, Bentheimer and Estaillades. The flow rates were varied such that they encompass flow regimes from Darcy to Forchheimer.

3.1. Darcy permeability and model comparison

At low velocity i.e., $Re_K \ll 1$, the Darcy permeabilities were calculated, see Table 2. The Darcy permeability of the beadpack can be predicted using the Kozeny–Carman equation

$$K_{\text{Kozeny–Carman}} = \frac{\phi^3}{S_v{}^2 \mathcal{K}(1-\phi)^2}, \tag{10}$$

where $\mathcal{K}$ is the Kozeny–Carman constant and S_v is the specific surface area. When the porous medium consists of spherical particles, $S_v = \frac{6}{D_p}$ where D_p is the particle diameter. $\mathcal{K} = 5$ applies for spheres [47]. The beadpack permeability approximation according to this yields $K_{\text{Kozeny–Carman}} = 6.255$ D which is similar to our result, 5.650 D, Table 2.

Table 2
Darcy flow parameters for the beadpack, Bentheimer and Estaillades calculated at low velocities.

Sample	Re_K	Pressure gradient (MPa/m)	K_D (D)
Beadpack	2.2×10^{-5}	16.67×10^{-4}	5.650
Bentheimer	4.4×10^{-6}	6.04×10^{-4}	3.547
Estaillades	4.3×10^{-8}	6.65×10^{-4}	0.172

3.2. Onset of non-Darcy flow

In Fig. 3, plots of pressure gradient as a function of volumetric velocity U are given showing nonlinear behaviour at high velocities; the onset of non-Darcy regime is also indicated.

In Fig. 4(a) the dimensionless permeabilities K^* for all samples are given as functions of Re_K depicting the transition from Darcy to non-Darcy flow. In Fig. 4(b) K^* is plotted as a function of Re_L. The critical Re_K and Re_L indicating the departure from Darcy flow for the beadpack, Bentheimer and Estaillades are shown in Table 3. Given that Re_K

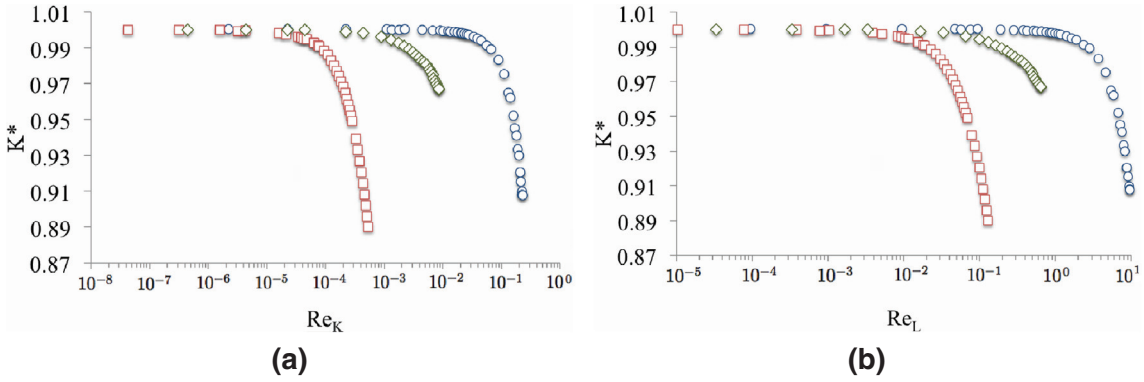

Fig. 4. The dimensionless permeability K^* as a function of (a) Re_K and (b) Re_L depicting the transition from the Darcy to non-Darcy flow regimes for Estaillades (□), Bentheimer (◇), and the beadpack (○).

Table 3
Predicted onsets of non-Darcy flow for the beadpack, Bentheimer and Estaillades.

Sample	Onset of non-Darcy flow	
	Re_K	Re_L
Beadpack	6.64×10^{-2}	2.79
Bentheimer	2.64×10^{-3}	0.196
Estaillades	9.4×10^{-5}	0.0226

is defined based on the Darcy permeabilities whereas Re_L on characteristic length, which is ambiguous for Bentheimer and Estaillades, Re_K can be viewed as the more physically consistent criterion for the onset of non-Darcy flow. From Table 3, it can be seen that the critical Reynolds number Re_K indicating the cessation of the Darcy regime for Estaillades is two orders of magnitude smaller than that for Bentheimer and is more than three orders of magnitude smaller than that for the beadpack.

In Table 4, the reported onsets of non-Darcy flow in several systems by several authors are given and compared to our computed onsets for the beadpack, Bentheimer and Estaillades. Apart from Ergun's formulation of Reynolds number which includes porosity ϕ, other authors formulated the Reynolds number as $Re = \frac{\rho D_p U}{\mu}$ which is our definition of Re_L. For the beadpack, our computations agree well with the estimations of Ergun [38], Scheiddeger [39] and Hassanizadeh and Gray [7] and deviate by less than one order of magnitude from the correlations of Fancher and Lewis [4] and Bear [6]. This shows that our numerically estimated onset of non-Darcy flow agrees well with experimental data conducted on similar systems. Fancher and Lewis [4] found that the onset for sandstone is between one to three orders of magnitude smaller than the onset for packed particles; we see a difference of approximately 25. Our predicted onset of non-Darcy flow for Estaillades does not fall within any of the published empirical results. However, none of the experiments was performed on carbonates with a complex pore structure. Our simulations indicate a much earlier onset of non-linear behaviour in samples with a tortuous pore structure.

3.3. Flow patterns and analysis

Several authors [5,12,42,44,45,48] have emphasised the effect of tortuosity on β factor. Although there has been no clear consensus in its definition, tortuosity has been generally defined as an average elongation of fluid paths within a porous medium. In practice tortuosity is difficult to obtain for complex geometries both experimentally and numerically. In the works of Duda et al. [49] and Koponen et al. [50], a method for computing tortuosity from the fluid velocity

Table 4
The onsets of non-Darcy flow as reported by several sources compared to our predictions (acquired at the point when $K^* = 0.99$) using the source's own definitions of Reynolds number.

Source	Criterion	Reported	Our predicted onset for:		
	Re	onset	Beadpack	Bentheimer	Estaillades
Chilton and Colburn [3]	$\frac{\rho D_p U}{\mu}$	40–80 (packed particles)	2.79	0.196	0.0226
Fancher and Lewis [4]	$\frac{\rho D_p U}{\mu}$	10–1000 (packed particles) 0.4–3 (sandstones)	2.79	0.196	0.0226
Ergun [38]	$\frac{\rho D_p U}{\mu(1-\phi)}$	3–10 (packed particles)	4.35	0.248	0.0253
Bear [6]	$\frac{\rho D_p U}{\mu}$	3–10 (packed particles)	2.79	0.196	0.0226
Scheidegger [39]	$\frac{\rho D_p U}{\mu}$	0.1–75 (packed particles)	2.79	0.196	0.0226
Hassanizadeh and Gray [7]	$\frac{\rho D_p U}{\mu}$	1–15 (packed particles)	2.79	0.196	0.0226

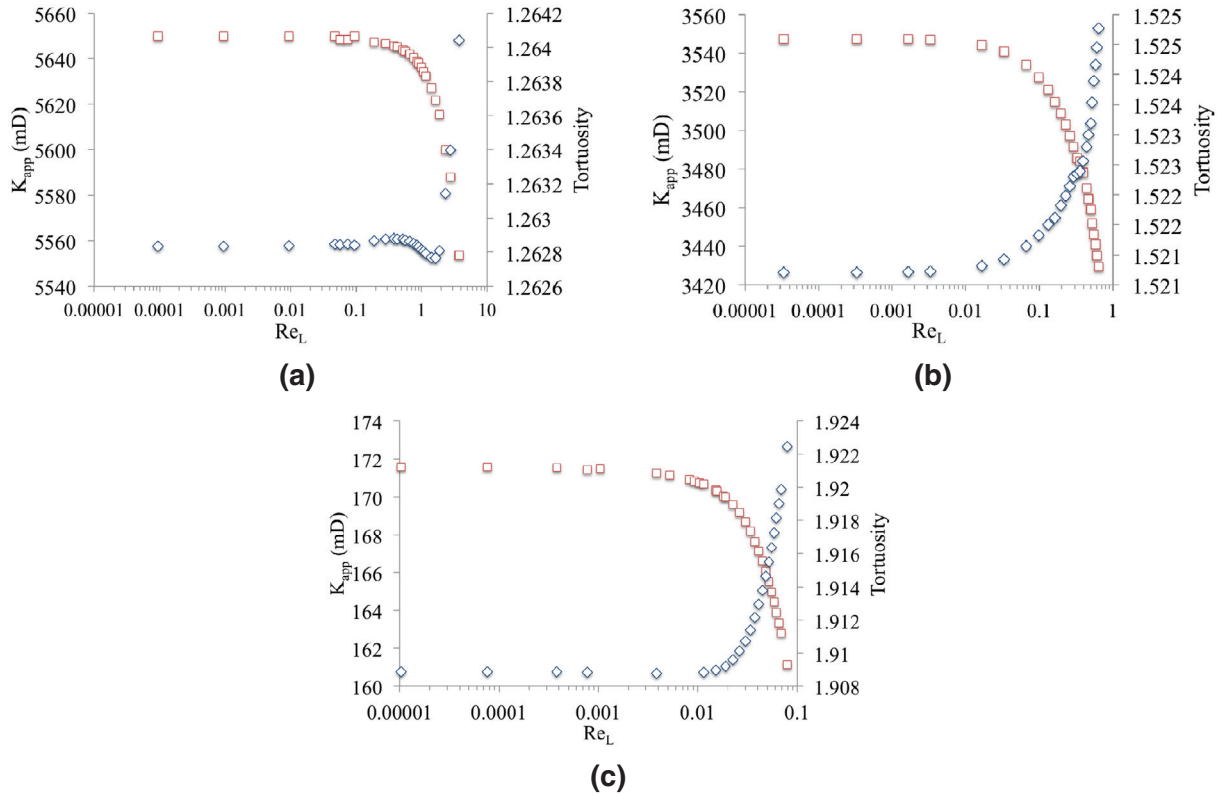

Fig. 5. Plots of tortuosities and apparent permeabilities K_{app} as functions of Re_L for (a) the beadpack, (b) Bentheimer, and (c) Estaillades. The symbol □ denotes K_{app} while the symbol ◇ denotes tortuosity.

field is proposed i.e.,

$$T = \frac{\langle \mathbf{u} \rangle}{\langle u_x \rangle} \geq 1 \tag{11}$$

where $\langle \mathbf{u} \rangle$ is the average magnitude of the intrinsic velocity over the entire system volume and $\langle u_x \rangle$ is the volumetric average of its component along the macroscopic flow direction. This method enables one to calculate tortuosity directly from the fluid velocity field, without the need to determine flowpaths.

Tortuosities and apparent permeabilities K_{app} for the three samples were computed and are plotted as functions of Re_L in Fig. 5. For Bentheimer and Estaillades, tortuosities show a monotonically increasing trend. For the beadpack, the tortuosity fluctuates slightly prior to increasing. This phenomenon has also been reported by Chukwudozie [51] in which the lattice Boltzmann method was employed to simulate non-Darcy flow through a body centred cubic sphere pack.

We can explain our results through studying the interstitial flow patterns in the different rock types and for different flow speeds. In Fig. 6, the flow streamlines[1] through the pore space of Estaillades at $Re_K = 3.17 \times 10^{-7}$, $Re_K = 3.154 \times 10^{-5}$ and $Re_K = 3.275 \times 10^{-4}$ are shown. These points represent flows at the Darcy stage ($K^* = 1$), early transition stage ($K^* = 0.995$) and in the Forchheimer flow regime ($K^* = 0.94$). In Fig. 6(a) the streamlines remain parallel to one another and their curvatures follow the form of the pores. In Fig. 6(b) steady eddies, where the streamlines move in closed circles, appear at some pores (circled). The emergence of these eddies coincides with a decrease of permeability and an increase of tortuosity. In Fig. 6(c) more steady eddies emerge in some pores and subsequently reduce the effective area available for flow.

In Fig. 7, the flow streamlines in Bentheimer at $Re_K = 4.45 \times 10^{-6}$, and $Re_K = 8.65 \times 10^{-3}$ are shown, while Fig. 8 illustrates the streamlines through the beadpack at $Re_K = 2.23 \times 10^{-3}$, and $Re_K = 2.06 \times 10^{-1}$. Unlike Estaillades, no eddies emerge within the pore spaces of Bentheimer or the beadpack even in the Forchheimer regime. Fourar et al. [10] pointed out that steady eddies are more likely to occur in porous media in which the grains touch and the flow pathways become more tortuous; for Estaillades we have the sample with the lowest porosity (most cemented pore space) and the largest tortuosity, see Fig. 5.

For the beadpack, Fig. 8(b), we see a very different behaviour, at much higher flow rates, during the Forchheimer regime. Flow appears to become focused in a straight high-speed zone, which is called an inertial core in [53]. In this more homogeneous system the changes in the flow paths are qualitatively different, with no eddies but rather an apparent concentration of fast flow.

In Fig. 9, we plot the velocity field in a centre plane of z-axis in the beadpack and compare it with the vector field of a beadpack acquired from a particle image velocimetry (PIV) measurement by Patil and Liburdy [40]. Their experiments were conducted on low aspect ratio porous beds (bed width-to-bead diameter) of 4.67 whereas our computational domain has an aspect ratio of 6. In their experiment, a pore Reynolds number, $Re_{\text{pore}} = 3.77$ was chosen[2] and we compare it with our simulation at $Re_{\text{pore}} = 3.85$ (equivalent to $Re_K = 0.088$) which is already in the transition to Forchheimer regime with $K^* = 0.983$. As

[1] Note that streamlines in a steady state flow are also pathlines. The streamlines can be computed from the velocity vector in every pore voxel; these were computed and plotted using ParaView [52].

[2] Patil and Liburdy [40] used the definition of pore Reynolds number $Re_{\text{pore}} = \frac{\rho U D_p}{\mu} \frac{2}{3} \frac{1}{(1-\phi)}$.

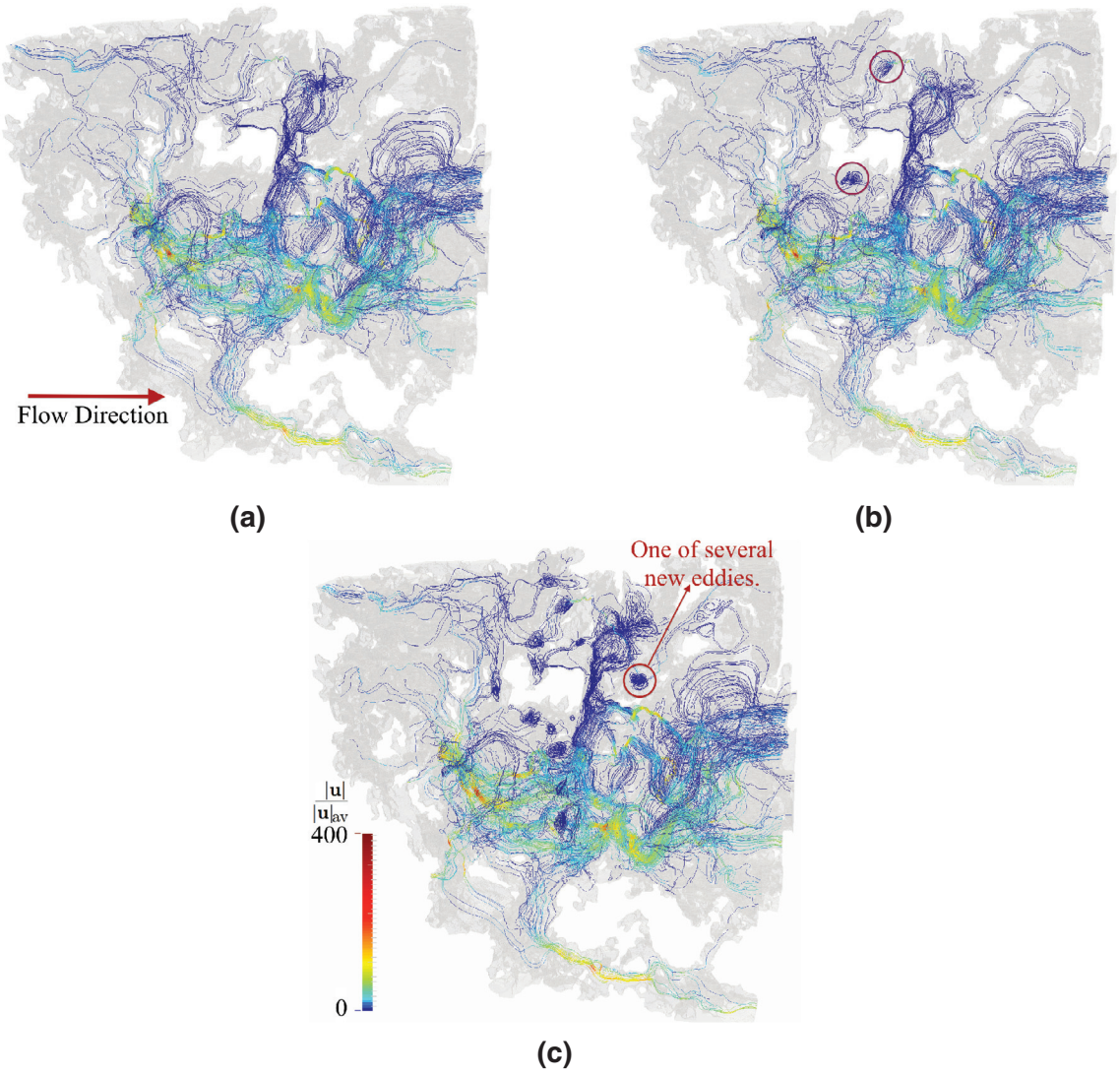

Fig. 6. Plots of flow streamlines within Estaillades pores (grey) at selected locations during (a) the Darcy regime ($Re_K = 3.17 \times 10^{-7}$), (b) the transition regime ($Re_K = 3.154 \times 10^{-5}$), and (c) the Forchheimer regime ($Re_K = 3.275 \times 10^{-4}$). The streamlines are coloured according to the ratios of the magnitude of velocity $|\mathbf{u}|$ at voxel centres to the average velocity $|\mathbf{u}|_{av}$ spanning from 0 to 400. The red circles indicate steady eddies the number and intensity of which increase markedly in the Forchheimer regime. (For interpretation of the references to colour in this figure legend, the reader is referred to the web version of this article.)

can be seen in the figures, both velocity fields show qualitatively no identifiable inertial structures formed such as flow separation nor recirculation regions. Several high velocity regions are seen, as a consequence of the three-dimensional flow geometry giving rapid flow into large pore spaces. While the results are not identical, since we study slightly different porous media, the overall features of the flow are similar, indicating that we correctly capture the key features of the flow field.

The turbulent flow regime is excluded in our simulations where the flow field varies in time, even in a steady-state regime; this regime has been considered using PIV measurements by [54,55].

3.4. β factor and model comparison

In Fig. 10, the inverse of apparent permeability $\frac{1}{K_{app}}$ is plotted as a function of $\frac{\rho U}{\mu}$. The β factors for the beadpack, Bentheimer and Estaillades are obtained from the slopes of these functions and are 2.57×10^5 m^{-1}, 2.07×10^6 m^{-1} and 6.15×10^8 m^{-1} for the beadpack, Bentheimer and Estaillades respectively.

Ergun [38] derived an empirical equation for approximating the β factor from an analysis of data from 640 experiments:

$$\beta_{\text{Ergun}} = \frac{14.2887}{K_D^{0.5}\phi^{1.5}}; \tag{12}$$

using SI units for β and K_D. For our beadpack sample (K_D from Table 2 is used while the porosity ϕ can be found in Table 1) $\beta_{\text{Ergun}} = 2.795 \times 10^5$ m^{-1}. This agrees well with our numerical estimation of β factor for beadpack, 2.57×10^5 m^{-1}.

Li and Engler [56] reviewed several empirical correlations for estimating β factor. We estimate the β factors for Bentheimer and Estaillades (the porosity ϕ can be found in Table 1 with the Darcy permeability K_D in Table 2). The tortuosities of the beadpack, Bentheimer and Estaillades are 1.26, 1.52 and 1.91 respectively. The estimated β factors in Table 5 vary between 0.36×10^6 and 13.71×10^6 m^{-1} for Bentheimer and between 0.61×10^8 and 24.77×10^8 m^{-1} for Estaillades. The wide range of these results does at least cover our numerical predictions of 2.07×10^6 m^{-1} for Bentheimer and 6.15×10^8 m^{-1} for Estaillades, although the 30-fold scatter does make quantitative use of the correlations problematic. Janicek and Katz [41] provide a good estimate for Bentheimer, while none of the correlations

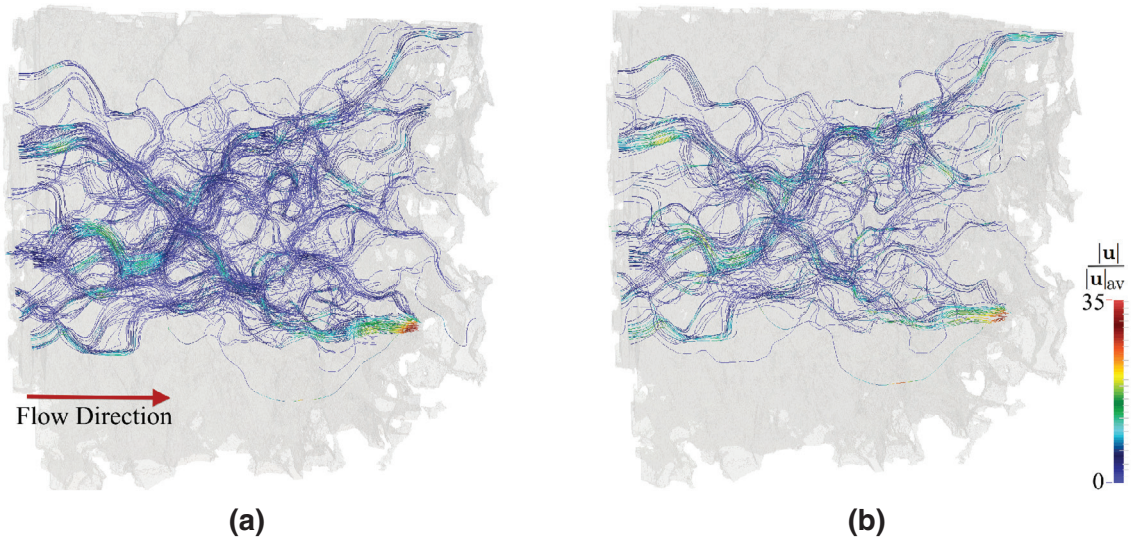

Fig. 7. Plots of flow streamlines within Bentheimer pores (grey) at selected locations during (a) the Darcy regime ($Re_K = 4.45 \times 10^{-6}$), and (b) the Forchheimer regime ($Re_K = 8.65 \times 10^{-3}$). The streamlines are coloured according to the ratios of the magnitude of velocity $|\mathbf{u}|$ at voxel centres to the average velocity $|\mathbf{u}|_{av}$ spanning from 0 to 35. In this case we do not see the development of eddies in the transition to the Forchheimer regime. (For interpretation of the references to colour in this figure legend, the reader is referred to the web version of this article.)

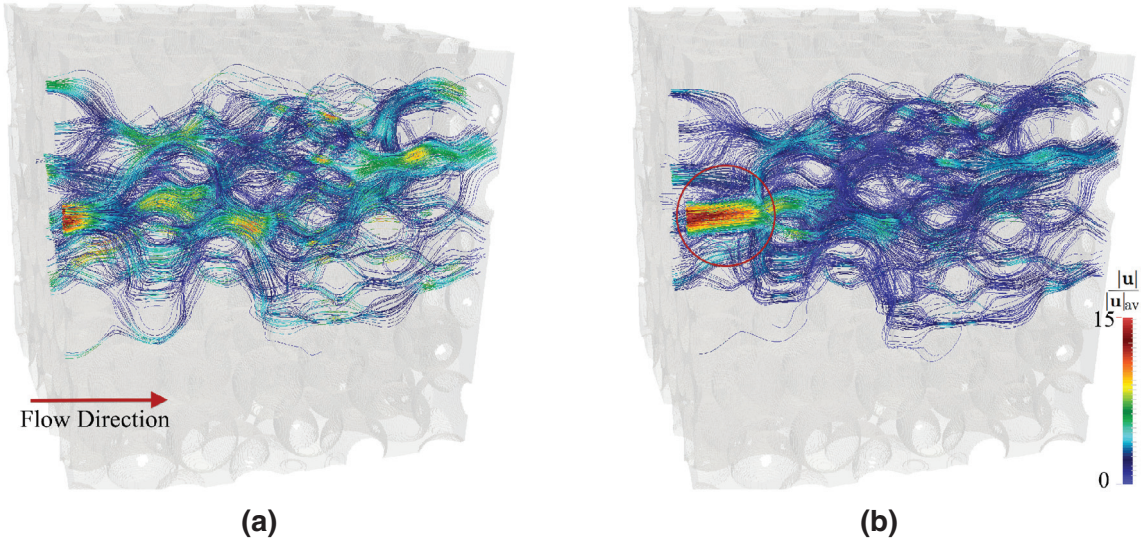

Fig. 8. Plots of flow streamlines within beadpack pores (grey) at selected locations during (a) the Darcy regime ($Re_K = 2.23 \times 10^{-3}$), and (b) the Forchheimer regime ($Re_K = 2.06 \times 10^{-1}$). The streamlines are coloured according to the ratios of the magnitude of velocity $|\mathbf{u}|$ at voxel centres to the average velocity $|\mathbf{u}|_{av}$ spanning from 0 to 15. The red circle indicates a focused region of fast flow. (For interpretation of the references to colour in this figure legend, the reader is referred to the web version of this article.)

provides accurate predictions for Estaillades. Indeed, this demonstrates the utility of our approach—to simulate flow directly in the system of interest.

3.5. Effects of grid refinement

An adequately resolved grid is particularly important for simulating flows within samples with small pore spaces and complex boundaries. In order to capture strong inertial effects which, for instance, manifest in delicate recirculation zones within Estaillades pores, one needs to employ sufficiently fine grids to minimize the effect of numerical errors.

To examine grid convergence, we re-run some of the flow cases within refined grids for the beadpack and Estaillades samples. For the beadpack image, we subdivide each voxel into eight smaller voxels of the same size to construct a new grid comprised of 600 × 600 × 600 voxels, each with a voxel size of 1 μm. For our Estaillades image, we subdivide each voxel in the same way and construct a new grid comprised of 1000 × 1000 × 1000 voxels with a voxel size of 1.655 μm.

We computed flows at five different Reynolds numbers for the beadpack i.e., $Re_K = 2.026 \times 10^{-6}$ and 2.026×10^{-3} which are in the Darcy regime; 2.022×10^{-2} and 7.3×10^{-2} which are in the transition regime; and 1.879×10^{-1} which is in the Forchheimer regime. For Estaillades, we performed simulations at $Re_K = 3.766 \times 10^{-8}$ and 3.750×10^{-5} which are in the Darcy regime; 7.454×10^{-5} and 1.001×10^{-4} which are in the transition regime; and 3.312×10^{-4} which is in the Forchheimer regime. The Darcy permeabilites computed in the refined grids are given in Table 6 and are compared with those computed in the original grids. The dimensionless apparent permeabilities as a function of Re_K computed in the original and in the refined grids are plotted in Fig. 12.

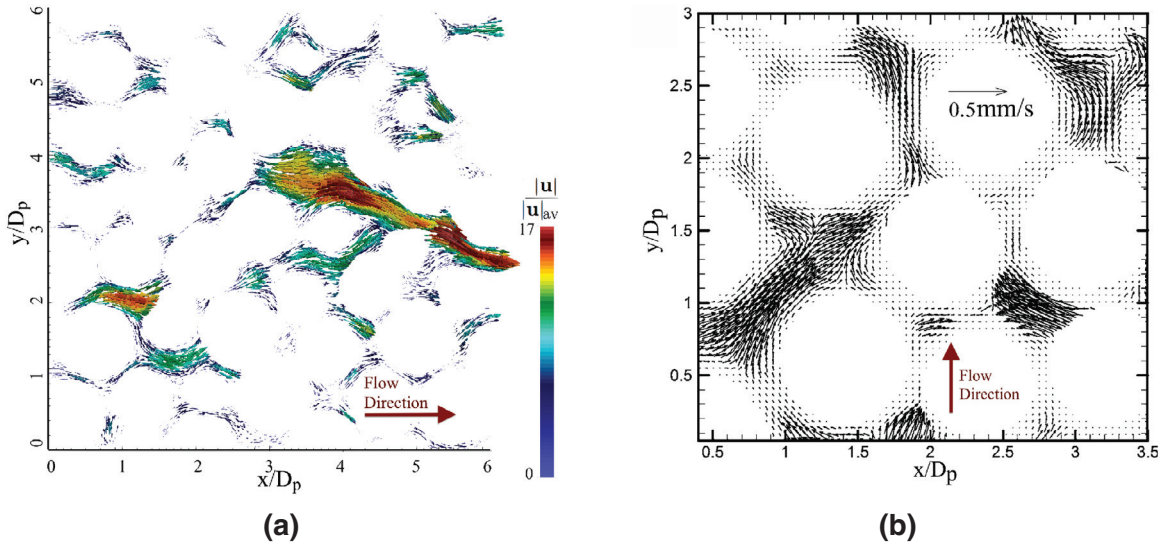

Fig. 9. The plots of (a) the velocity field in the beadpack, generated on the centre plane $z = 300\ \mu m$ at $Re_{pore} = 3.85$ ($Re_K = 0.088$), compared to (b) the velocities obtained using a PIV measurement of steady-state flow in a beadpack at $Re_{pore} = 3.77$ by Patil and Liburdy [40]. Both fields show no signs of flow separation nor recirculation regions. Several very high velocity regions are seen, as a consequence of the three-dimensional flow geometry causing flow into large pore spaces.

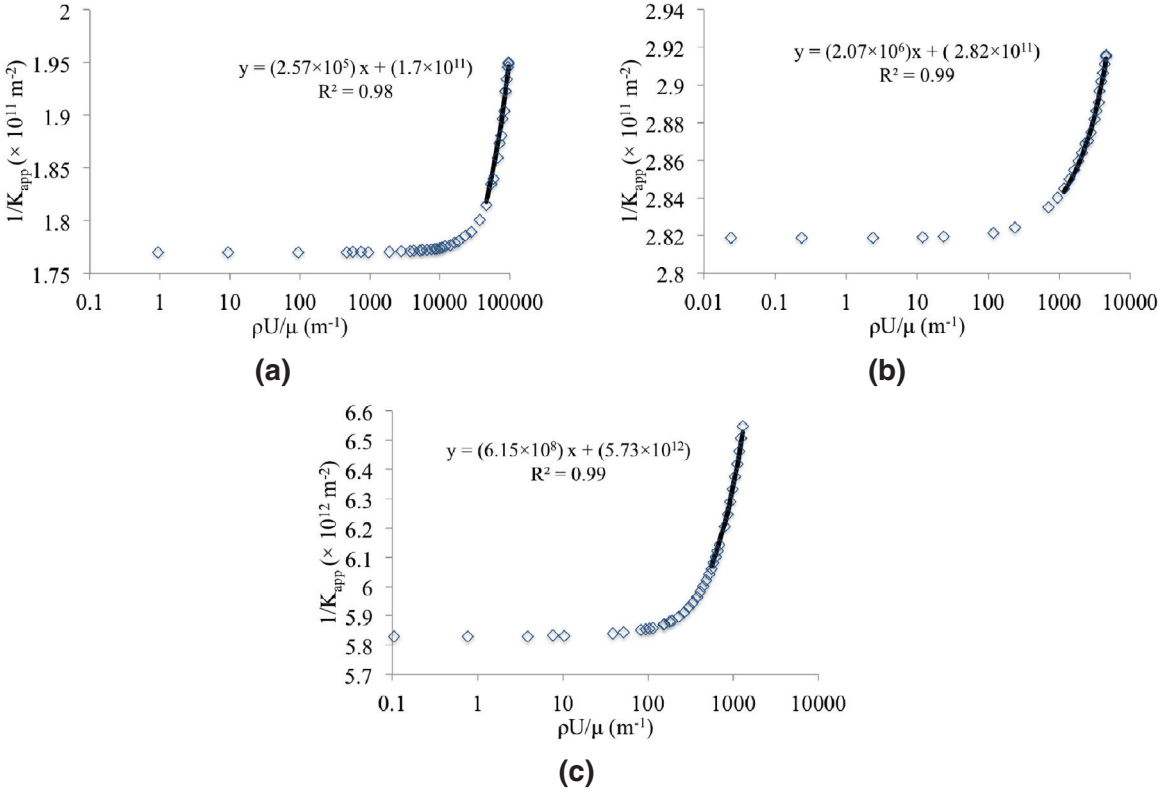

Fig. 10. Forchheimer graphs for (a) the beadpack, (b) Bentheimer, and (c) Estaillades where $\frac{1}{K_{app}}$ is plotted as a function of $\frac{\rho U}{\mu}$. β factors are obtained from the slopes of the graphs i.e., $2.57 \times 10^5\ m^{-1}$ for the beadpack, $2.07 \times 10^6\ m^{-1}$ for Bentheimer and $6.15 \times 10^8 m^{-1}$ for Estaillades.

The Darcy permeabilities computed in the refined grids compare well with those computed in the original grids; they vary less than 5%. Such a variation is consistent with the fact that new voxels could have given a way for new flow paths to emerge, as studied in [18]. To illustrate this, we plot the streamlines in both the original and refined grids of Estaillades pores at the Forchheimer regime, see Fig. 11. Although there are additional flow paths in the refined grid, which now consists of 8-times as many voxels as the original grid, the main flow patterns in both grids are comparable.

When a comparison between the data computed in the original and the refined grids is made in terms of dimensionless apparent permeabilities K^* as functions of Re_K, see Fig. 12, the data computed in the refined grid are in excellent agreement with the trend of the data computed in the original grid in the Darcy, transition and in the Forchheimer regimes; both predict consistent onsets of the non-Darcy flow. These results suggest that we have used sufficiently refined grids to describe the transition from Darcy to Forchheimer flow.

Table 5
β factors for Bentheimer (with $K_D = 3.547 \times 10^{-12}$ m^2, $\phi = 0.211$, and tortuosity = 1.52) and β factors of Estaillades (with $K_D = 1.716 \times 10^{-13}$ m^2, $\phi = 0.108$, and tortuosity = 1.91) approximated using the empirical correlations proposed by different authors. Our simulated values of β factors are 2.07×10^6 m^{-1} for Bentheimer, and 6.15×10^8 m^{-1} for Estaillades.

Source	Empirical model β	Units of β and K_D	Bentheimer $\beta \times 10^6$ m^{-1}	Estaillades $\beta \times 10^8$ m^{-1}
Janicek and Katz [41]	$\frac{1.82 \times 10^8}{K_D^{5/4}\phi^{3/4}}$	cm^{-1}, mD	2.09	1.53
Jones [8]	$\frac{6.15 \times 10^{10}}{K_D^{1.55}}$	ft^{-1}, mD	0.62	0.68
Cooper et al. [42]	$\frac{10^{-3.25}T^{1.943}}{K_D^{1.023}}$	cm^{-1}, mD	5.32	1.83
Geertsma [43]	$\frac{0.005}{K_D^{0.5}\phi^{5.5}}$	cm^{-1}, cm^2	13.71	24.77
Liu et al. [44]	$\frac{8.91 \times 10^8 T}{K_D\phi}$	ft^{-1}, mD	5.85	2.97
Thauvin and Mohanty [12]	$\frac{1.55 \times 10^4 T^{3.35}\phi^{0.29}}{K_D^{0.98}}$	cm^{-1}, D	2.84	1.43
Coles and Hartman [45]	$\frac{1.07 \times 10^{12}\phi^{0.449}}{K_D^{1.88}}$	ft^{-1}, mD	0.36	0.79
Li et al. [46]	$\frac{11500}{\phi K_D}$	cm^{-1}, D	1.52	0.61

Table 6
Comparison of Darcy permeabilities computed in the original and in the refined grids of the beadpack, and Estaillades. The results are in good agreement varying less than 5%.

	Beadpack		Estaillades	
	Original grid	Refined grid	Original grid	Refined grid
Image size	$300 \times 300 \times 300$	$600 \times 600 \times 600$	$500 \times 500 \times 500$	$1000 \times 1000 \times 1000$
Voxel size (μm)	2	1	3.31	1.65
K_D (D)	5.650	5.386	0.173	0.167

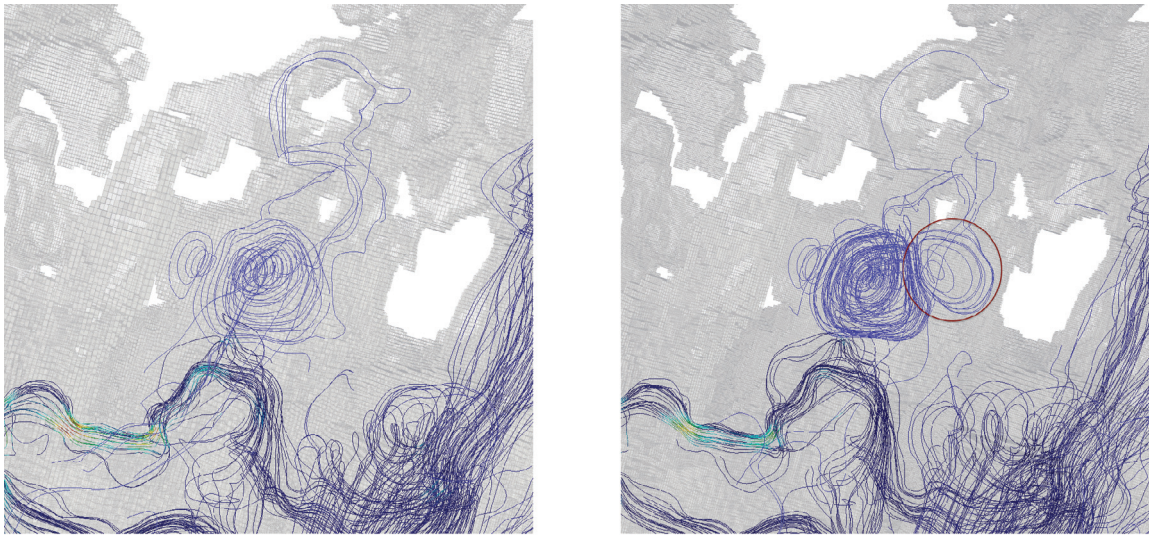

Fig. 11. Plots of streamlines within Estaillades pores (grey) at selected locations during the Forchheimer regime computed in (a) the original grid, $500 \times 500 \times 500$ voxels, at $Re_K = 3.275 \times 10^{-4}$, and (b) the refined grid, $1000 \times 1000 \times 1000$ voxels, at $Re_K = 3.3125 \times 10^{-4}$. Although additional flow paths are exhibited in the refined grid, the main flow characteristics in both grids are comparable.

4. Concluding remarks

- In this study, the effect of pore-scale heterogeneity on the onset of non-Darcy flow has been investigated by means of direct flow simulations through 3D images of a beadpack, Bentheimer sandstone and Estaillades carbonate. The onset of non-Darcy flow is defined as the point when the dimensionless apparent permeability $K^* = 0.99$; using this criterion our analysis shows that the critical Reynolds number Re_K indicating the onset of non-Darcy flow for Estaillades is two orders of magnitude smaller than that for Bentheimer and three orders of magnitude smaller than that for the beapack.
- The wide pore size distribution of Estaillades, as studied in [14], combined with poor connectivity helps initiate the emergence

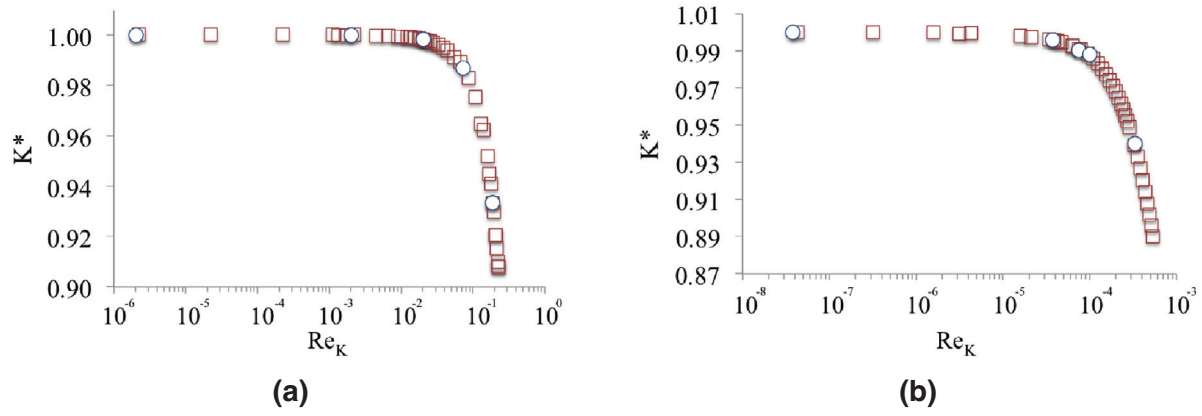

Fig. 12. The dimensionless permeability K^* as a function of Re_K depicting the transition from the Darcy to non-Darcy flow regimes for (a) the beadpack, and (b) Estaillades. Symbol (□) represents the data computed in the original grid i.e., 300 × 300 × 300 for the beadpack (voxel size = 2 μm), and 500 × 500 × 500 for Estaillades (voxel size = 3.31 μm); whereas symbol (○) represents the data computed in the refined grid i.e., 600 × 600 × 600 for the beadpack (voxel size = 1 μm), and 1000 × 1000 × 1000 for Estaillades (voxel size = 1.655 μ m).

of steady eddies which increases tortuosity, and reduces the effective area available for flow, triggering the departure from the Darcy regime. In contrast, eddies do not emerge within Bentheimer nor the beadpack. In beadpack, the appearance of a fast flow path characterizes the emergence of the Forchheimer regime, and at much higher Reynolds numbers than seen in the carbonate.

- Our calculation of the Darcy permeability of the beadpack agrees within around 20% with the Kozeny–Carman equation. Our predicted β factor for the beadpack is also in good agreement with the Ergun estimation. Our predicted β factors for Bentheimer sandstone and Estaillades carbonate have been compared to experimental data from various authors and are broadly comparable, although none of the experiments was specifically conducted on Bentheimer or Estaillades.
- The predicted onsets of non-Darcy flow for the beadpack, Bentheimer and Estaillades have been compared to available experimental data. For the beadpack, a very good agreement is found. Fancher and Lewis [4] noted a smaller critical Reynolds number for sandstone compared to packed particles, which is also what we observed. The onset of non-Darcy flow for Estaillades does not match the prediction of the available experimental data, none of which relates to Estaillades, and which indicates that the onset may be very sensitive to the details of the pore structure in very heterogeneous rocks.
- We suggest the use of the permeability-based Reynolds number Re_K and the dimensionless permeability K^* proposed by Newman and Yin [11] for predicting the onset of non-Darcy flow given their sound physical meaning and convenience when used to compare non-Darcy flow parameters of samples with different heterogeneities.
- X-ray imaging technology used along with direct numerical simulation is a viable alternative to experiments or empirical models for estimating macroscopic parameters of non-Darcy flow such as the β factor, permeability, tortuosity and the onset of non-Darcy flow.

Acknowledgements

We would like to thank the Engineering and Physical Science Research Council for financial support through grant no. EP/L012227/1. In compliance with RCUK policy on Open Access applies for EPSRC funded research, the images of Estaillades carbonate, Bentheimer sandstone and beadpack are available through: https://www.imperial.ac.uk/engineering/departments/earth-science/research/research-groups/perm/research/pore-scale-modelling/micro-ct-images-and-networks/.

References

[1] Dupuit J. Èstudes thèoriques et pratiques sur le mouvement des eaux, Paris: Dunod; 1863. ISBN-10: 0543975029, ISBN-13: 978-0543975027.
[2] Forchheimer P. Wasserbewegung durch boden. Zeit Ver Deutsch Ing 1901(45):1781–8.
[3] Chilton TH, Colburn AP. Pressure drop in packed tubes. Ind Eng Chem 1931;23(8):913–19. http://dx.doi.org/10.1021/ie50260a016.
[4] Fancher HG, Lewis AJ. Flow of simple fluids through porous materials. Ind Eng Chem 1933;25(10):1139–47. http://dx.doi.org/10.1021/ie50286a020.
[5] Green Jr L, Duwez P. Fluid flow through porous metals. J Appl Mech 1951;39(18):39–45.
[6] Bear J. Dynamics of fluids in porous media. Dover Publications; 1972. ISBN 978-0-486-65675-5.
[7] Hassanizadeh S, Gray W. High velocity flow in porous media. Transp Porous Media 1987;2(6):521–31. http://dx.doi.org/10.1007/BF00192152.
[8] Jones SC. Using the inertial coefficient, β, to characterize heterogeneity in reservoir rock. In: SPE annual technical conference and exhibition, SPE-16949-MS. Society of Petroleum Engineers; 1987. http://dx.doi.org/10.2118/16949-MS.
[9] Al-Rumhy MH, Kalam MZ. Relationship of core-scale heterogeneity with non-Darcy flow coefficients. SPE J 1996;11:108–13. http://dx.doi.org/10.2118/25649-PA.
[10] Fourar M, Radilla G, Lenormand R, Moyne C . On the non-linear behavior of a laminar single-phase flow through two and three-dimensional porous media. Adv Water Resour 2004;27(6):669–77. http://dx.doi.org/10.1016/j.advwatres.2004.02.021.
[11] Newman MS, Yin X. Lattice Boltzmann simulation of non-Darcy flow in stochastically generated 2D porous media geometries. SPE J 2013;18:12–26. http://dx.doi.org/10.2118/146689-PA.
[12] Thauvin F, Mohanty K . Network modeling of non-Darcy flow through porous media. Transp Porous Media 1998;31(1):19–37. http://dx.doi.org/10.1023/A:1006558926606.
[13] Bijeljic B, Raeini A, Mostaghimi P, Blunt MJ . Predictions of non-Fickian solute transport in different classes of porous media using direct simulation on pore-scale images. Phys Rev E 2013;87:013011. http://dx.doi.org/10.1103/PhysRevE.87.013011.
[14] Bijeljic B, Mostaghimi P, Blunt MJ. Insights into non-Fickian solute transport in carbonates. Water Resour Res 2013;49(5):2714–28. http://dx.doi.org/10.1002/wrcr.20238.
[15] Siena M, Riva M, Hyman JD, Winter CL, Guadagnini A. Relationship between pore size and velocity probability distributions in stochastically generated porous media. Phys Rev E 2014;89:013018. http://dx.doi.org/10.1103/PhysRevE.89.013018.
[16] Hyman JD, Smolarkiewicz PK, Winter CL. Heterogeneities of flow in stochastically generated porous media. Phys Rev E 2012;86:056701. http://dx.doi.org/10.1103/PhysRevE.86.056701.
[17] Sukop MC, Huang H, Alvarez PF, Variano EA, Cunningham KJ. Evaluation of permeability and non-Darcy flow in Vuggy Macroporous limestone aquifer samples with lattice Boltzmann methods. Water Resour Res 2013;49(1):216–30. http://dx.doi.org/10.1029/2011WR011788.
[18] Chukwudozie CP, Tyagi M, Sears SO, White CD. Prediction of non-Darcy coefficients for inertial flows through the castlegate sandstone using image-based modeling. Transp Porous Media 2012;95(3):563–80. http://dx.doi.org/10.1007/s11242-012-0062-5.
[19] Finney JL. Random packings and the structure of simple liquids. I. the geometry of random close packing. Proc R Soc London A: Math, Phys Eng Sci 1970;319(1539):479–93. http://dx.doi.org/10.1098/rspa.1970.0189.
[20] Prodanović M, Bryant SL. A level set method for determining critical curvatures for drainage and imbibition. J Colloid Interface Sci 2006;304(2):442–58. http://dx.doi.org/10.1016/j.jcis.2006.08.048.

[21] Guadagnini A, Blunt M, Riva M, Bijeljic B. Statistical scaling of geometric characteristics in millimeter scale natural porous media. Transp Porous Media 2014;101(3):465–75. http://dx.doi.org/10.1007/s11242-013-0254-7.
[22] Hilfer R. Review on scale dependent characterization of the microstructure of porous media. Transp Porous Media 2002;46(2-3):373–90. http://dx.doi.org/10.1023/A:1015014302642.
[23] Buades A, Coll B, Morel J-M. A non-local algorithm for image denoising. In: IEEE computer society conference on computer vision and pattern recognition, 2005 (CVPR 2005), 2; 2005. p. 60–5. http://dx.doi.org/10.1109/CVPR.2005.38.
[24] Buades A, Coll B, Morel J-M. Nonlocal image and movie denoising. Int J Comput Vis 2008;76(2):123–39. http://dx.doi.org/10.1007/s11263-007-0052-1.
[25] Andrew M, Bijeljic B, Blunt MJ. Pore-scale imaging of trapped supercritical carbon dioxide in sandstones and carbonates. Int J Greenhouse Gas Control 2014;22:1–14. http://www.sciencedirect.com/science/article/pii/S1750583613004519. http://dx.doi.org/10.1016/j.ijggc.2013.12.018.
[26] Mostaghimi P, Bijeljic B, Blunt M. Simulation of flow and dispersion on pore-space images. SPE J 2012;17:1131–41. http://dx.doi.org/10.2118/135261-PA.
[27] Issa RI. Solution of the implicitly discretised fluid flow equations by operator-splitting. J Comput Phys 1986;62(1):40–65. http://dx.doi.org/10.1016/0021-9991(86)90099-9.
[28] Raeini AQ, Blunt MJ, Bijeljic B. Modelling two-phase flow in porous media at the pore scale using the volume-of-fluid method. J Comput Phys 2012;231(17):5653–68. http://dx.doi.org/10.1016/j.jcp.2012.04.011.
[29] Kwak D. Numerical simulations of incompressible flows. World Scientific; 2003. ISBN 9789812796837 https://books.google.co.uk/books?id=LfhxhLySDecC.
[30] Angrand F, Institut National de Recherces en Informatique et Automatique Workshop. Numerical methods for the Euler equations of fluid dynamics. Proceedings in applied mathematics series. Society for Industrial and Applied Mathematics; 1985. ISBN 9780898712001 https://books.google.co.uk/books?id=RzABBbx4obMC.
[31] Jasak H. Error analysis and estimation for the finite volume method with applications to fluid flows. Imperial College London; 1996. (Ph.D. thesis).
[32] Weller HG, Tabor G, Jasak H, Fureby C. A tensorial approach to computational continuum mechanics using object-oriented techniques. Comput Phys 1998;12(6):620–31. http://dx.doi.org/10.1063/1.168744.
[33] Guibert R, Nazarova M, Horgue P, Hamon G, Creux P, Debenest G. Computational permeability determination from pore-scale imaging: sample size, mesh and method sensitivities. Transp Porous Media 2015;107(3):641–56. http://dx.doi.org/10.1007/s11242-015-0458-0.
[34] Chhabra R. Bubbles, drops, and particles in non-Newtonian fluids. 2nd ed. Chemical Industries/Taylor & Francis; 2006. ISBN 9781420015386.
[35] Comiti J, Sabiri N, Montillet A. Experimental characterization of flow regimes in various porous media III: limit of Darcy's or creeping flow regime for Newtonian and purely viscous non-Newtonian fluids. Chem Eng Sci 2000;55(15):3057–61. http://dx.doi.org/10.1016/S0009-2509(99)00556-4.
[36] Zeng Z, Grigg R. A Criterion for Non-Darcy Flow in Porous Media. Transp Porous Media 2006;63(1):57–69. http://dx.doi.org/10.1007/s11242-005-2720-3.
[37] Durlofsky L, Brady JF. Analysis of the brinkman equation as a model for flow in porous media. Phys Fluids 1987;30(11):3329–41. http://dx.doi.org/10.1063/1.866465.
[38] Ergun S. Fluid flow through packed columns. Chem Eng Progress 1952;48(2):89–94. http://dx.doi.org/10.1021/ie50474a011.
[39] Scheidegger A. The physics of flow through porous media. University of Toronto Press; 1974. ISBN 9780802018496.
[40] Patil V, Liburdy J . Flow characterization using PIV measurements in a low aspect ratio randomly packed porous bed. Exp Fluids 2013a;54(4):1497. http://dx.doi.org/10.1007/s00348-013-1497-3.
[41] Janicek J, Katz D. Applications of unsteady state gas flow calculations. In: Proceedings of University of Michigan research conference; 1955.
[42] Cooper JW, Wang X, Mohanty KK. Non-Darcy-flow studies in anisotropic porous media. SPE J 1999;4:334–41. http://dx.doi.org/10.2118/57755-PA.
[43] Geertsma J. Estimating the coefficient of inertial resistance in fluid flow through porous media. SPE J 1974;14:445–50. http://dx.doi.org/10.2118/4706-PA.
[44] Liu X, Civan F, Evans RD. Correlation of the non-Darcy flow coefficient. J Can Petrol Technol 1995;34. http://dx.doi.org/10.2118/95-10-05.
[45] Coles ME, Hartman KJ. Non-Darcy measurements in dry core and the effect of immobile liquid. In: SPE gas technology symposium, SPE-39977-MS. Society of Petroleum Engineers; 1998. http://dx.doi.org/10.2118/39977-MS.
[46] Li D, Svec RK, Engler TW, Grigg RB. Modeling and simulation of the wafer non-Darcy flow experiments. In: SPE western regional meeting, SPE-68822-MS. Society of Petroleum Engineers; 2001. http://dx.doi.org/10.2118/68822-MS.
[47] Kececioglu I, Jiang Y. Flow through porous media of packed spheres saturated with water. J Fluids Eng 1994;116(March):164–70. http://dx.doi.org/10.1115/1.2910229.
[48] Ruth D, Ma H. On the derivation of the Forchheimer equation by means of the averaging theorem. Transp Porous Media 1992;7(3):255–64. http://dx.doi.org/10.1007/BF01063962.
[49] Duda A, Koza Z, Matyka M. Hydraulic tortuosity in arbitrary porous media flow. Phys Rev E 2011;84:036319. http://dx.doi.org/10.1103/PhysRevE.84.036319.
[50] Koponen A, Kataja M, Timonen J. Tortuous flow in porous media. Phys Rev E 1996;54:406–10. http://dx.doi.org/10.1103/PhysRevE.54.406.
[51] Chukwudozie CP. Pore-scale lattice Boltzmann simulations of inertial flows in realistic porous media: a first principle analysis of the Forchheimer Relationship. Louisiana State University; 2011. (Master thesis).
[52] Henderson A, Ahrens J. The Paraview guide: a parallel visualization application, New York: Kitware, Inc.; 2004. ISBN 1-930934-14-9 http://opac.inria.fr/record=b1117983.
[53] Dybbs A, Edwards R. A new look at porous media fluid mechanics Darcy to turbulent. In: Bear J, Corapcioglu M, editors. Fundamentals of transport phenomena in porous media. NATO ASI Series, vol. 82. Netherlands: Springer; 1984. p. 199–256. ISBN 978-94-009-6177-7. http://dx.doi.org/10.1007/978-94-009-6175-3_4.
[54] Patil VA, Liburdy JA. Turbulent flow characteristics in a randomly packed porous bed based on particle image velocimetry measurements. Phys Fluids (1994-present) 2013;25(4):043304. http://dx.doi.org/10.1063/1.4802043.
[55] Patil VA, Liburdy JA. Flow structures and their contribution to turbulent dispersion in a randomly packed porous bed based on particle image velocimetry measurements. Phys Fluids (1994-present) 2013;25(11):113303. http://dx.doi.org/10.1063/1.4832380.
[56] Li D, Engler TW. Literature review on correlations of the non-Darcy coefficient. In: SPE permian basin oil and gas recovery conference, SPE-70015-MS. Society of Petroleum Engineers; 2001. http://dx.doi.org/10.2118/70015-MS.